water

MDPI

Article

High-Resolution Modeling and Diagnostic Assessment of Theoretical Tidal Current Energy Resources in the Bohai and Yellow Seas

Zhenlu Wang [1], Bo Jing [2], Xingyu Xu [3,4,*], Ning Yuan [5], Luming Shi [1] and Bingchen Liang [1]

[1] College of Engineering, Ocean University of China, Qingdao 266100, China; wangzhenlu@ouc.edu.cn (Z.W.); shiluming@ouc.edu.cn (L.S.); bingchen@ouc.edu.cn (B.L.)
[2] Sinopec Shengli Oilfield, Dongying 257000, China; jingbo_sl@hotmail.com
[3] Sinopec Shengli Oilfield Branch Technical Testing Center, Dongying 257000, China
[4] Sinopec (Shandong) Testing and Evaluation Research Co., Ltd., Dongying 257000, China
[5] Laoshan Laboratory, Qingdao 266237, China; nyuan@lsnl.cn
* Correspondence: xuxingyu.slyt@sinopec.com

Abstract

The global transition to a diversified renewable energy portfolio requires reliable assessment of predictable marine energy resources. This study develops a high-resolution, three-dimensional Regional Ocean Modeling System (ROMS) to quantitatively evaluate theoretical tidal current energy resources in the Bohai and Yellow Seas. The model, configured with fine-scale bathymetry and forced by harmonic tidal constituents, is validated against tide gauge and Acoustic Doppler Current Profiler (ADCP) observations. Multi-year simulations reveal pronounced spatial heterogeneity in tidal current energy distribution. Rather than treating resource assessment as a single power density mapping exercise, this study combines annual mean theoretical power density, peak theoretical power density, threshold-dependent effective flow duration, effective water depth, current directionality, and vertical velocity structure to characterize resource intensity, temporal persistence, and vertical deployability. The results identify distinct hydrodynamic resource regimes. High theoretical resource intensity is concentrated west of Laotieshan Cape and east of Chengshantou, where cumulative annual effective flow duration exceeds 5000 h and short-term instantaneous theoretical power density can reach approximately 10 kW/m^2 and 8 kW/m^2, respectively. These peak values indicate strong local tidal acceleration but should be interpreted together with annual mean power density and effective flow duration. In contrast, the northern Jiangsu coastal area exhibits lower peak intensity but relatively persistent moderate flow conditions. The results provide a hydrodynamic resource basis for preliminary site screening and for guiding subsequent turbine-performance, wake/array, environmental, grid accessibility, and techno-economic assessments.

Keywords: tidal current energy; Bohai Sea; Yellow Sea; numerical simulation; multi-index diagnostic assessment

Check for updates

Academic Editors: Yonggang Lu, Yandong Gu, Wenwu Zhang and Yongyao Luo

Received: 6 May 2026
Revised: 28 May 2026
Accepted: 5 June 2026
Published: 11 June 2026

Copyright: © 2026 by the authors. Licensee MDPI, Basel, Switzerland. This article is an open access article distributed under the terms and conditions of the Creative Commons Attribution (CC BY) license.

1. Introduction

The urgent transition from fossil fuels to renewable energy is critical for achieving global carbon-neutrality goals. Ocean energy—including tidal power—has emerged as a promising renewable resource due to its vast potential and unique characteristics [1,2]. In particular, tidal current energy offers a dual advantage of high predictability (owing to its

astronomical forcing) and high power density [1,3]. Tidal-stream generation is exceptionally clean, with emissions on the order of ~1.8 gCO_2/kWh (much lower than wind or solar) [2,3]. Global studies estimate that the tidal current power resource could supply on the order of 1200 TWh per year (≈4% of current world electricity demand) [2,4,5]. These factors have led many countries (e.g., UK, Canada, France, Korea) to include tidal energy in their decarbonization strategies [1,5].

Regions characterized by broad shallow seas, complex coastlines, and numerous channels often exhibit intensified tidal currents suitable for energy extraction [6,7]. The Bohai and Yellow Seas, situated on the eastern continental shelf of China, represent one such area. Their particular geomorphology, featuring headlands, straits, and semi-enclosed bays, creates hydrodynamic conditions conducive to the acceleration of tidal flows [7–9]. Consequently, this region has been identified as a prospective area for tidal current energy development, with several studies indicating the presence of localized high-velocity currents [7–9]. Accurate and high-fidelity quantification of the tidal energy resource in this area is therefore of fundamental importance for advancing marine renewable energy science and informing potential development.

Tidal energy resource assessment typically follows two approaches: in situ measurement and numerical simulation [6,10]. Direct observations (e.g., tide gauges or moored ADCP current profilers) can accurately capture site-specific currents, but they are expensive, limited in spatial coverage, and provide only point information [10]. Consequently, numerical modeling is widely used to map the resource over large areas. Mature ocean circulation models—such as the Regional Ocean Modeling System (ROMS), the Finite-Volume Community Ocean Model (FVCOM), or the Princeton Ocean Model (POM)—have been applied successfully to simulate tidal dynamics and currents in coastal seas [10–13]. For example, Robins et al. used a high-resolution ROMS simulation to characterize tidal-stream energy resources over shelf seas [13], while elsewhere, POM has been applied to strait channels [12]. High-resolution unstructured models like FVCOM are also capable of resolving complex coastlines and fine bathymetry, enabling detailed assessments of tidal power potential [11].

Many numerical case studies illustrate the above methods. Globally, resource assessments have been carried out at site and national scales [1,14]. In Asia, recent modeling efforts have focused on specific regions. For instance, Yuan et al. performed a 3D hydrodynamic simulation for the Bohai and Yellow Seas, harmonic analysis, and flux methods to estimate the extractable current power, identifying peak power densities of ~6.2 kW/m^2 (east of Shandong) and ~5.5 kW/m^2 (Bohai Strait) [8]. Other Chinese studies have assessed tidal energy around Weihai and Hulu Island, finding similarly high-energy channels [15,16]. A coupled wind–wave–current model for the Yellow–Bohai Sea further confirmed that this region is rich in renewable energy [7]. These works have identified key development zones (e.g., Laotieshan, Chengshantou, Daqing Channel) and provided first-order estimates of the local tidal resource [7,8,15,16].

Despite these advances, several aspects of regional tidal current energy assessment in the Bohai and Yellow Seas remain insufficiently characterized. First, many previous studies have focused mainly on the spatial distribution of current speed or mean power density, whereas less attention has been paid to the combined description of resource intensity, temporal persistence, and vertical deployability. Temporal variability is particularly important for tidal-stream energy assessment because spring-neap modulation, diurnal inequality, and tidal asymmetry may influence the practical interpretation of resource persistence and potential power generation [13]. Second, site suitability is not determined by current magnitude alone. Water depth and depth-related deployability are also important factors in tidal-stream site screening, especially in depth-limited coastal regions [17,18]. Third, previous estimates are not always directly comparable because model resolution,

bathymetric datasets, open-boundary tidal forcing, and the statistical definitions of mean or peak resource metrics can influence simulated current magnitude and derived power density [19]. Therefore, a high-resolution, multi-year, three-dimensional diagnostic assessment is still needed to characterize not only the magnitude of the theoretical tidal current resource, but also its persistence, effective water depth, vertical structure, and hotspot-scale hydrodynamic differences.

In light of these issues, the present study does not claim methodological novelty from the use of ROMS itself, because ROMS and other hydrodynamic models have been widely applied to tidal current simulations and resource assessments [10,13]. Instead, the contribution of this work lies in applying a high-resolution, multi-year, three-dimensional diagnostic framework to characterize the theoretical tidal current energy resource of the Bohai and Yellow Seas. Following the general concept of theoretical tidal current resource characterization recommended in IEC TS 62600-201:2015 [20], this framework integrates four complementary aspects: (1) spatial mapping of annual mean and peak theoretical power density; (2) evaluation of threshold-dependent effective flow duration to characterize resource persistence; (3) estimation of effective water depth to represent the vertical extent of potentially usable currents; and (4) hotspot-scale analysis of current directionality and vertical velocity structure.

The objectives of this study are therefore to: (1) identify the spatial heterogeneity of theoretical tidal current energy in the Bohai and Yellow Seas using a high-resolution three-dimensional hydrodynamic model; (2) distinguish different hydrodynamic resource regimes by jointly considering resource intensity, persistence, effective water depth, and vertical structure; and (3) provide a preliminary hydrodynamic resource basis for subsequent turbine-performance, environmental, and techno-economic assessments, rather than directly estimating technically extractable or economically recoverable energy.

2. Materials and Methods

This study employs the Regional Ocean Modeling System (ROMS, version 3.9), an open-source, three-dimensional ocean circulation model widely used for regional marine numerical simulations. The model is based on the free surface and terrain-following coordinate system, solving the three-dimensional Reynolds-averaged Navier–Stokes equations under the Boussinesq and hydrostatic approximations using a finite-difference scheme. It is capable of accurately simulating the evolutionary characteristics of regional-scale ocean dynamic processes. ROMS supports structured grid construction, effectively adapts to complex topographic boundaries, and maintains good numerical stability with high spatial resolution, making it suitable for various marine environments such as coastal waters, continental shelves, and estuaries. Its design emphasizes modularity and couplability, allowing flexible integration with subsystems like the atmosphere and waves to simulate multi-physical field interactions and feedback mechanisms. In this research, the ROMS model is utilized to construct a high-resolution, long-term time series tidal current field for the Bohai and Yellow Seas, providing fundamental data for the dynamic assessment and spatiotemporal distribution analysis of tidal current energy resources.

2.1. Governing Equations

In the Cartesian coordinate system, the ROMS momentum equations can be expressed as follows:

$$\frac{\partial u}{\partial t} + \vec{\nabla}\cdot\nabla u - fv = -\frac{\partial \phi}{\partial x} - \frac{\partial}{z}\left(\overline{u'w'} - \nu\frac{\partial u}{\partial z}\right) + F_u + D_u, \quad (1)$$

$$\frac{\partial v}{\partial t} + \vec{\nabla}\cdot\nabla v + fu = -\frac{\partial \phi}{\partial y} - \frac{\partial}{z}\left(\overline{v'w'} - \nu\frac{\partial v}{\partial z}\right) + F_v + D_v, \quad (2)$$

Under the Boussinesq approximation, density variations are retained only in the buoyancy term of the momentum equation. Combined with the hydrostatic assumption, this leads to a balance in the vertical direction between the vertical pressure gradient and the buoyancy force.

$$\frac{\partial \Phi}{\partial z} = -\frac{\rho g}{\rho_0}, \tag{3}$$

Continuity Equation for Incompressible Flow,

$$\frac{\partial u}{\partial x} + \frac{\partial v}{\partial y} + \frac{\partial w}{\partial z} = 0, \tag{4}$$

In the oceanic environment, the contribution of vertical molecular diffusion to mixing processes is typically negligible compared to that of turbulent mixing. Consequently, terms containing the molecular viscosity (ν) and diffusivity (ν_θ) coefficients in the ROMS governing equations can be neglected. To achieve closure of the equation set, the model introduces parameterizations for the Reynolds stress tensor and the turbulent tracer fluxes. These unclosed turbulent flux terms are solved via a turbulence closure scheme, which effectively simulates the feedback of small-scale oceanic turbulence on the larger-scale flow structure. The specific expressions are given below.

$$\overline{u'w'} = -K_M \frac{\partial u}{\partial z}, \tag{5}$$

$$\overline{v'w'} = -K_M \frac{\partial v}{\partial z}, \tag{6}$$

Vertical boundary conditions at the sea surface ($z = \eta(x, y, t)$):

$$K_M \frac{\partial u}{\partial z} = \tau_s^{\mathrm{x}}(x, y, t) \ , \tag{7}$$

$$K_M \frac{\partial v}{\partial z} = \tau_s^{\mathrm{y}}(x, y, t) \ , \tag{8}$$

$$w = \frac{\partial \eta}{\partial_{\mathrm{t}}} \ , \tag{9}$$

Vertical boundary conditions at the sea bottom ($z = -h(x, y)$):

$$K_M \frac{\partial u}{\partial z} = \tau_b^x(x, y, t), \tag{10}$$

$$-w + \vec{V} \cdot \nabla h = 0, \tag{11}$$

2.2. Terrain-Following Coordinate System

ROMS employs a terrain-following S-coordinate system. The Cartesian coordinate system and the S-coordinate system differ only in their vertical coordinate. Two methods are available for transforming the vertical coordinate z from the Cartesian system to the S-coordinate s. Furthermore, ROMS provides two forms of this coordinate transformation, along with four options for the vertical stretching functions.

Transformation Form 1 (corresponding to parameter V-transform = 1):

$$z(x, y, \sigma, t) = S(x, y, \sigma) + \eta(x, y, t)\left[1 + \frac{S(x, y, \sigma)}{h(x, y)}\right], \tag{12}$$

$$S(x, y, \sigma) = h_c \sigma + [h(x, y) - h_x] C(\sigma), \tag{13}$$

$$S(x, y, \sigma) = \begin{cases} 0, & when\ \sigma = 0, C(\sigma) = 0\ at\ the\ sea\ surface \\ -h(x, y), & when\ \sigma = -1, C(\sigma) = -1\ at\ the\ sea\ bottom \end{cases}, \tag{14}$$

Transformation Form 2 (corresponding to parameter V-transform = 2):

$$z(x,y,\sigma,t) = \eta(x,y,t) + [\eta(x,y,t) + h(x,y)]S(x,y,\sigma), \tag{15}$$

$$S(x,y,\sigma) = \frac{h_c\sigma + h(x,y)C(\sigma)}{h_c + h(x,y)}, \tag{16}$$

$$S(x,y,\sigma) = \begin{cases} 0, & when\ \sigma = 0, C(\sigma) = 0\ at\ the\ sea\ surface \\ -h(x,y), & when\ \sigma = -1, C(\sigma) = -1\ at\ the\ sea\ bottom \end{cases}, \tag{17}$$

Stretching Scheme 1 (corresponding to parameter V-stretching = 1):

$$C(\sigma) = (1-\theta_B)\frac{\sin h(\theta_S\sigma)}{\sin h(\theta_S)} + \theta_B\left[\frac{tanh\left[\theta_S\left(\sigma+\frac{1}{2}\right)\right]}{2tanh\left(\frac{1}{2}\theta_S\right)} - \frac{1}{2}\right], \tag{18}$$

Here, θ_S and θ_B are the surface and bottom control parameters, respectively. Their value ranges are $0 \le \theta_S \le 20$ and $0 \le \theta_B \le 1$. They possess the following characteristics: a larger θ_S leads to higher vertical resolution in the water column above the critical depth h_c. When $\theta_B = 0$, increasing θ_S causes the resolution throughout the water column to become more concentrated near the surface. When $\theta_B = 1$, the resolution near both the surface and bottom increases proportionally with θ_S. It is recommended that $\theta_S \le 8$ when $\theta_B \ne 0$.

Stretching Scheme 2 (corresponding to parameter V-stretching = 2):

$$C(\sigma) = \mu C_{sur}(\sigma) + (1-\mu)C_{bot}(\sigma), \tag{19}$$

$$C_{sur}(\sigma) = \frac{1-\cos h(\theta_S\sigma)}{\cos h(\theta_S) - 1}, \theta_S > 0, \tag{20}$$

$$C_{bot}(\sigma) = \frac{\sin h[\theta_B(\sigma+1)]}{\sin h(\theta_B)} - 1, \theta_B > 0, \tag{21}$$

$$\mu = (\sigma+1)^{\alpha}\left[1 + \frac{\alpha}{\beta}\left(1-(\sigma+1)^{\beta}\right)\right], \tag{22}$$

Stretching Scheme 3 (corresponding to parameter V-stretching = 3, R. Geyer function):

$$C(\sigma) = \mu C_{bot}(\sigma) + (1-\mu)C_{sur}(\sigma), \tag{23}$$

$$C_{sur}(\sigma) = -\frac{\log\left[\cos h\left(\gamma abs(\sigma)^{\theta_s}\right)\right]}{\log[\cos h(\gamma)]}, \tag{24}$$

$$C_{bot}(\sigma) = \frac{\log[\cos h(\gamma(\sigma+1)^{\theta_B})]}{\log[\cos h(\gamma)]} - 1, \tag{25}$$

$$\mu = \frac{1}{2}\left[1 - tanh\left(\gamma\left(\sigma+\frac{1}{2}\right)\right)\right], \tag{26}$$

$$\gamma = 3, \tag{27}$$

Stretching Scheme 4 (corresponding to parameter V-stretching = 4):

$$C(\sigma) = \frac{1-\cos h(\theta_S\sigma)}{\cos h(\theta_S) - 1}, \theta_S > 0, \tag{28}$$

$$C(\sigma) = -\sigma^2, \theta_S \le 0, \tag{29}$$

$$C(\sigma) = \frac{\exp(\theta_B C(\sigma)) - 1}{1 - \exp(-\theta_B)}, \theta_B > 0, \tag{30}$$

$$0 \le \theta_S \le 10, 0 \le \theta_B \le 4, \tag{31}$$

After the vertical coordinate transformation, the ROMS governing equations in the S-coordinate system are expressed as follows:

$$\frac{\partial u}{\partial t} + \vec{\nabla}\cdot\nabla u - fv = -\frac{\partial \Phi}{\partial x} - \left(\frac{g\rho}{p_0}\right)\frac{\partial z}{\partial x} - g\frac{\partial \eta}{\partial x} + \frac{1}{H_z}\frac{\partial}{\partial \sigma}\left[\frac{(K_M + v)}{H_z}\frac{\partial u}{\partial \sigma}\right] + F_u + D_u, \tag{32}$$

$$\frac{\partial v}{\partial t} + \vec{\nabla}\cdot\nabla v + fu = -\frac{\partial \Phi}{\partial y} - \left(\frac{g\rho}{p_0}\right)\frac{\partial z}{\partial y} - g\frac{\partial \eta}{\partial y} + \frac{1}{H_z}\frac{\partial}{\partial \sigma}\left[\frac{(K_M + v)}{H_z}\frac{\partial v}{\partial \sigma}\right] + F_v + D_v, \tag{33}$$

$$\frac{\partial \Phi}{\partial \sigma} = \left(\frac{-gH_z\rho}{\rho_0}\right), \tag{34}$$

$$\frac{\partial H_z}{\partial t} + \frac{\partial (H_z u)}{\partial x} + \frac{\partial (H_z v)}{\partial y} + \frac{\partial (H_z \omega)}{\partial \sigma} = 0, \tag{35}$$

where $H_z = \frac{\partial z}{\partial \sigma}$. The relationship between the vertical velocity in the S-coordinate system (ω) and that in the Cartesian system (w) is given by the following:

$$w(x, y, \sigma, t) = \frac{1}{H_z}\left[w - \frac{z + h}{\eta + h}\frac{\partial \eta}{\partial t} - u\frac{\partial z}{\partial x} - v\frac{\partial z}{\partial y}\right], \tag{36}$$

$$w = \frac{\partial z}{\partial t} + u\frac{\partial z}{\partial x} + v\frac{\partial z}{\partial y} + wH_z, \tag{37}$$

In the S-coordinate system, the vertical boundary condition at the free surface ($\sigma = 0$) is expressed as follows:

$$\left(\frac{K_M}{H_z}\right)\frac{\partial u}{\partial \sigma} = \tau_s^x(x, y, t), \tag{38}$$

$$\left(\frac{K_M}{H_z}\right)\frac{\partial v}{\partial \sigma} = \tau_s^y(x, y, t), \tag{39}$$

$$w = 0, \tag{40}$$

The vertical boundary condition at the sea bottom ($\sigma = -1$) is expressed as follows:

$$\left(\frac{K_M}{H_z}\right)\frac{\partial u}{\partial \sigma} = \tau_b^x(x, y, t), \tag{41}$$

$$\left(\frac{K_M}{H_z}\right)\frac{\partial v}{\partial \sigma} = \tau_b^y(x, y, t), \tag{42}$$

$$w = 0, \tag{43}$$

2.3. Numerical Grid

In the horizontal direction, ROMS employs a curvilinear orthogonal structured grid (Figure 1), which is adaptable to common coordinate systems such as Cartesian, polar, and spherical coordinates. The model's state variables are discretized on an Arakawa C-grid staggering arrangement. The free surface elevation η, density ρ, and active/passive tracers are positioned at the center of grid cells, while the horizontal velocity components (u and v) are located at the western/eastern and southern/northern cell faces, respectively.

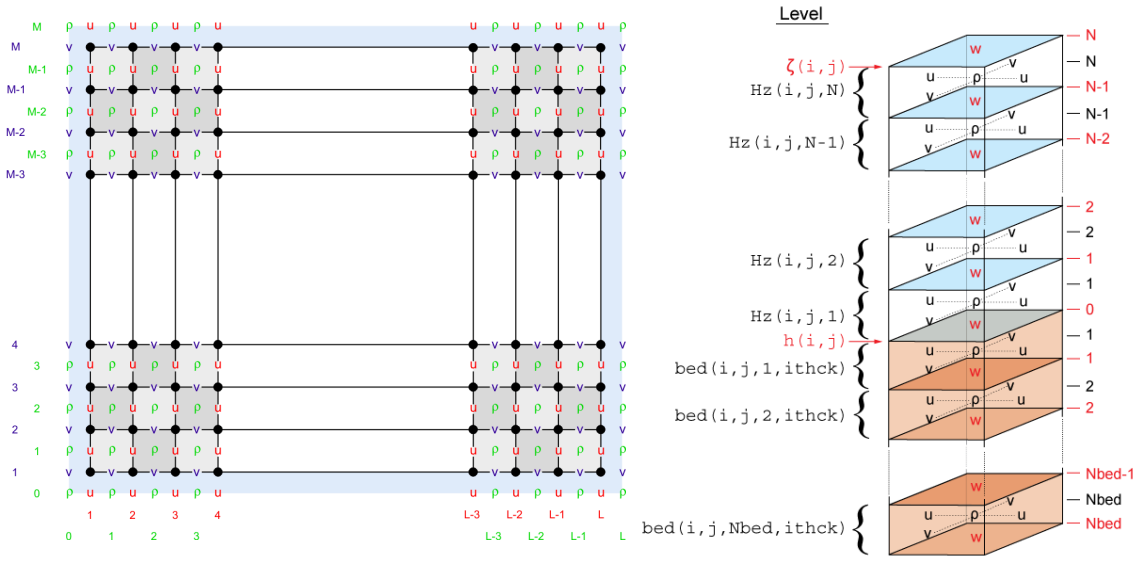


Figure 1. The horizontal C-grid and vertical grid distributions in the ROMS.

In the vertical direction, ROMS utilizes a terrain-following, stretched vertical coordinate system to accommodate complex bathymetry. This coordinate framework allows for flexible vertical discretization of the governing equations, ensuring refined resolution in both the bottom boundary layer and surface mixed layer. The thickness of vertical grid cells varies with topography and local water depth, meaning the vertical layer structure differs across horizontal grid points. Within a three-dimensional grid cell, the free surface and density remain at the cell center. The zonal (u) and meridional (v) velocities are situated on the cell faces in the north–south and east–west directions, respectively, whereas the vertical velocity (w) and vertical mixing coefficients are defined at the top and bottom cell interfaces. The horizontal index ranges are [0:L, 1:M] for zonal variables and [1:L, 0:M] for meridional variables, with L and M denoting the grid dimensions. The vertical velocity and mixing parameters range over [0, N]. The total water column thickness is given by $\zeta(i,j) + h(i,j)$, where the still water depth h remains temporally invariant unless morphodynamic feedback is activated.

3. Development and Validation of a Tidal Current Energy Calculation Model

3.1. Computational Grid and Boundary Conditions

Based on the three-dimensional Regional Ocean Modeling System (ROMS), a numerical simulation system for tidal current energy in the Bohai and Yellow Seas was constructed. The computational domain encompasses the entire Bohai and Yellow Seas, with the model grid illustrated in Figure 2. A curvilinear orthogonal grid was employed, featuring a horizontal spatial resolution that gradually increases from approximately 3 km in the open sea to 1 km in nearshore areas to enhance the resolution of complex coastal hydrodynamic processes. For bathymetry, the General Bathymetric Chart of the Oceans (GEBCO) global dataset was applied to offshore regions (water depth > 30 m), while 2017 national nautical chart data were used for shallow coastal zones. Data from these different sources were merged using a linear scatter interpolation method, and a nine-point smoothing algorithm was applied to the depth gradients to ensure numerical stability and physical soundness.

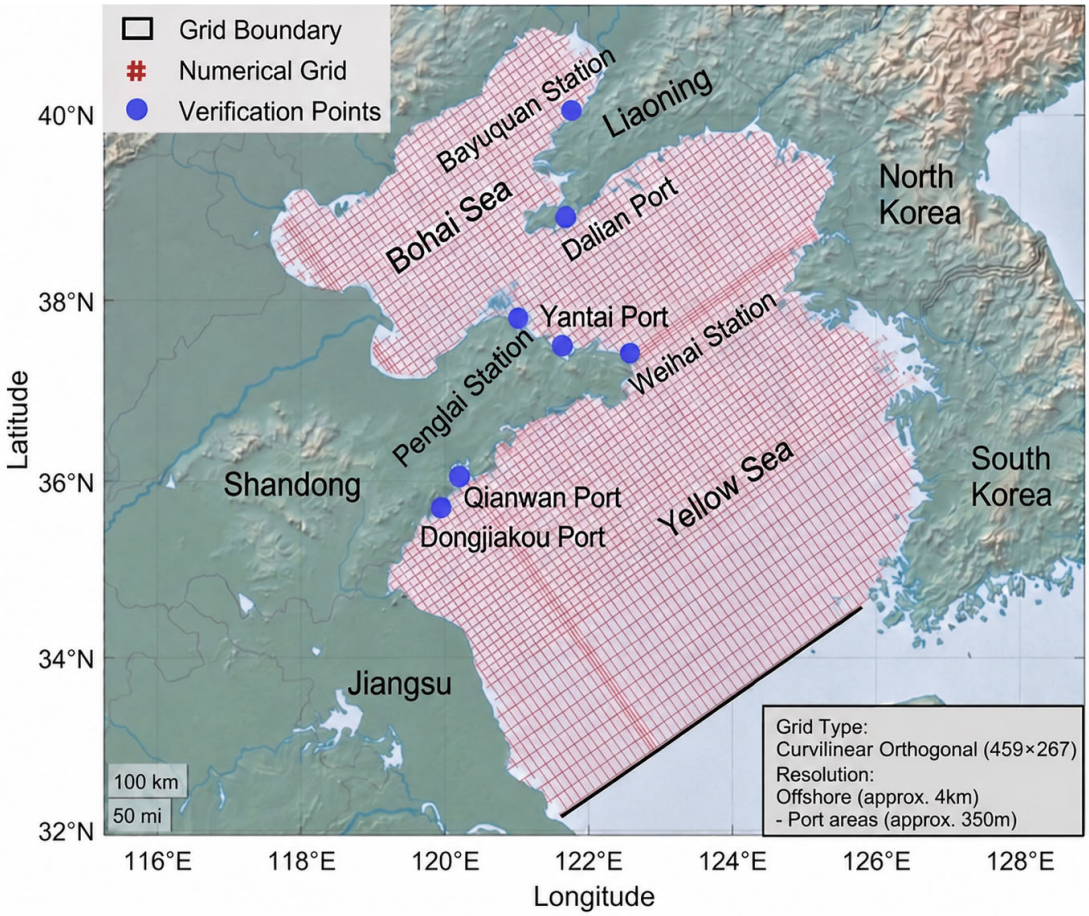


Figure 2. Computational grid for ROMS model.

The southern boundary of the model was configured as an open boundary. Tidal elevation and velocity information at this boundary were derived by superimposing data from the global TPXO tidal model and the HYCOM global hybrid-coordinate ocean reanalysis product to ensure a physically sound representation of large-scale tidal and circulation features. Atmospheric forcing was introduced via surface wind stress, calculated from 10 m wind speed data obtained from the ECMWF Reanalysis v5 (ERA5). Key physical parameterizations include: horizontal viscosity and diffusion coefficients set to 0.001 m^2/s and 0.1 m^2/s, respectively; vertical mixing parameterized using the K-Profile Parameterization (KPP) scheme with optimized mixed layer and turbulence parameters; background vertical diffusion coefficients for temperature and momentum set to 1.0×10^{-6} m^2/s and 1.0×10^{-5} m^2/s, respectively; bottom friction formulated via a logarithmic boundary layer law with dynamic adjustment based on substrate properties and local flow fields; and surface forcing driven by ERA5-derived fields including wind, atmospheric pressure, and heat fluxes. The open boundary implements a Radiation Boundary Condition combined with a Flather condition for the propagation of surface elevation and velocity. Initial conditions for velocity and elevation were extracted from HYCOM reanalysis data and mapped onto the model grid via bilinear interpolation. To enhance computational efficiency and stability, a split-explicit method was adopted, with time steps of 15 s for the external mode and 30 s for the internal mode. Model outputs were saved hourly to meet the temporal resolution requirements for subsequent spatiotemporal analysis of tidal current energy resources.

Although the model grid provides regional-scale high-resolution coverage of the Bohai and Yellow Seas, some very narrow channels, steep bathymetric gradients, small embayments, and artificial coastal structures may still be insufficiently resolved. Because

tidal acceleration near headlands and straits is sensitive to bathymetric gradients and coastline geometry, hotspot-scale current magnitude and derived power density may be affected by grid resolution and bathymetric smoothing. In addition, bottom friction parameterization, vertical turbulence closure, and open-boundary tidal forcing may also influence simulated current speed. These factors are therefore considered important sources of uncertainty in the interpretation of local power density estimates.

The inclusion of HYCOM background fields and ERA5 atmospheric forcing allows the model to represent large-scale circulation and wind-driven variability to some extent. However, the present study is primarily designed for regional-scale theoretical tidal current energy assessment. It does not include a dedicated sensitivity analysis of seasonal stratification, river discharge variability, or monsoon-driven residual circulation. Therefore, the simulated resource patterns should be interpreted mainly as tide-dominated hydrodynamic resource characteristics, while the influence of seasonal hydrographic processes is discussed as an uncertainty source.

3.2. Model Validation

To evaluate the reliability of the established ROMS model for tidal current energy assessment, both tidal elevation and current velocity validations were conducted. Tidal-gauge observations were used to examine the model capability in reproducing regional tidal propagation, amplitude, and phase, while ADCP current observations were used to evaluate the simulated depth-averaged current speed and direction. The comparison shows that the model successfully captured the variation trends of astronomical tides at all stations (Figure 3). The correlation coefficients (R) all exceeded 0.95, indicating a strong linear consistency between the simulated and observed time series. The mean absolute error (MAE) remained below 0.10 m, and the root mean square error (RMSE) was controlled within 0.12 m, demonstrating the model's high accuracy in simulating tidal amplitudes.

Further harmonic analysis was performed on the tidal level series using the T_TIDE toolbox. The results confirmed that the tidal system in the Bohai and Yellow Seas is dominated by the M_2 constituent (the principal semi-diurnal tide), followed by diurnal constituents such as K_1 and O_1, which is consistent with the regional tidal dynamics. A station-by-station comparison of the simulated and observed amplitudes for the major tidal constituents (M_2, K_1, O_1) is provided in Tables 1–3. The simulated amplitudes agree well with the observations, with all relative errors within 10%. Although the amplitude of the dominant M_2 constituent was slightly underestimated, the deviation remained within an acceptable error margin. These results collectively verify the model's reliable capability in reproducing astronomical tidal dynamics.

Table 1. Comparison of simulated astronomical tide constituent amplitudes vs. observed values at Qingdao Dongjiakou Sea.

Tidal Constituent	Observed Amplitude (m)	Simulated Amplitude (m)
M_2	1.45	1.37
S_2	0.51	0.40
K_1	0.29	0.20
O_1	0.23	0.21
N_2	0.24	0.22
K_2	0.21	0.13
P_1	0.10	0.17
Q_1	0.03	0.03

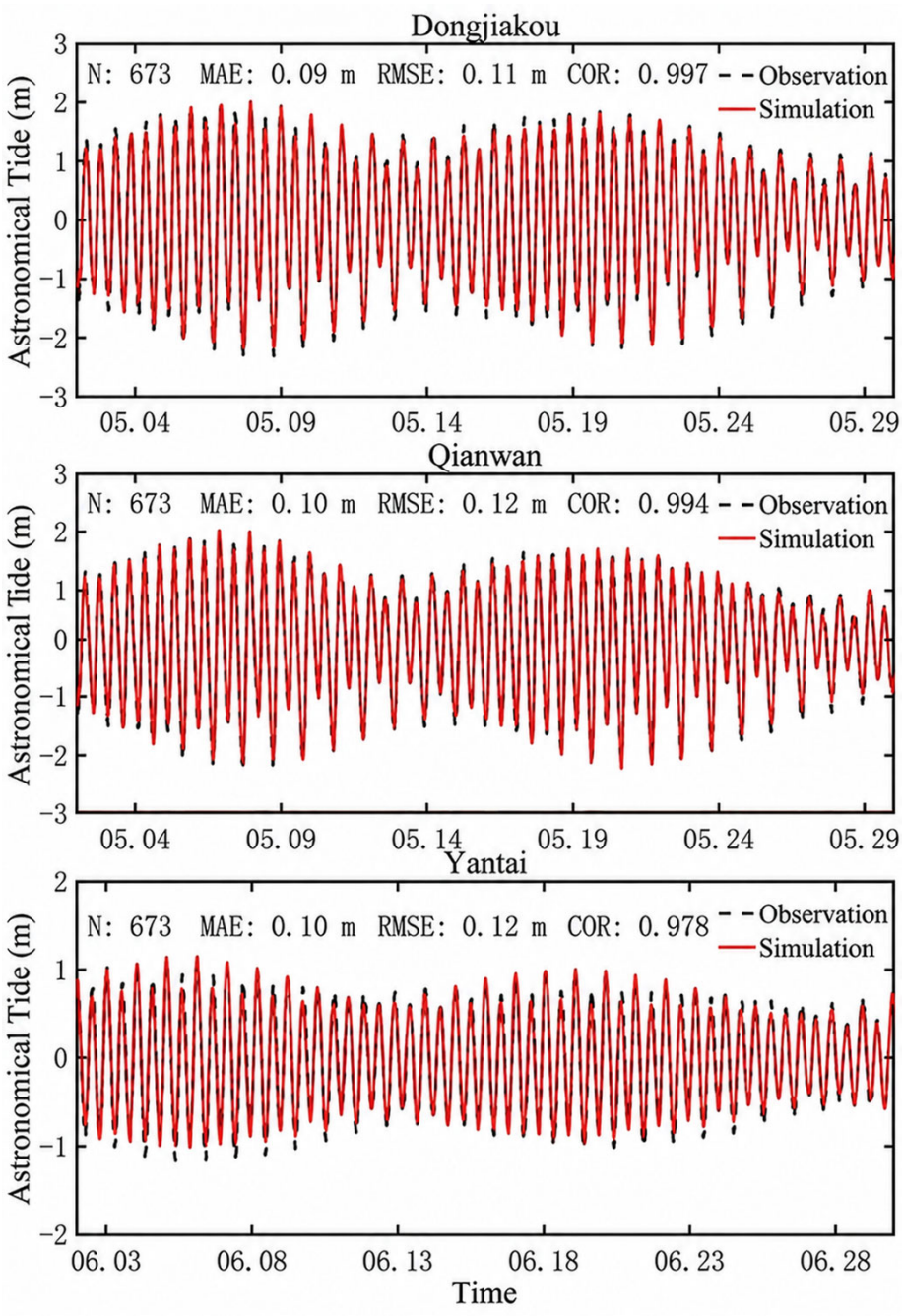


Figure 3. Comparisons of modeled and observed tidal elevations at validation points.

Table 2. Comparison of simulated astronomical tide constituent amplitudes vs. observed values at Qingdao Qianwan Area.

Tidal Constituent	Observed Amplitude (m)	Simulated Amplitude (m)
M_2	1.34	1.28
S_2	0.52	0.38
K_1	0.25	0.19
O_1	0.21	0.21
N_2	0.21	0.20
K_2	0.21	0.11
P_1	0.10	0.16
Q_1	0.03	0.03

Table 3. Comparison of simulated astronomical tide constituent amplitudes vs. observed values at Yantai Harbor Area.

Tidal Constituent	Observed Amplitude (m)	Simulated Amplitude (m)
M_2	0.78	0.75
S_2	0.32	0.29
K_1	0.12	0.13
O_1	0.05	0.04
N_2	0.13	0.11
K_2	0.12	0.08
P_1	0.04	0.03
Q_1	0.00	0.01

For the validation of the simulated tidal current fields, three representative stations—Bayuquan, Weihai, and Penglai—were selected to compare the modeled and observed depth-averaged current velocities and directions (Figures 4 and 5). The results show that the root mean square error (RMSE) of the depth-averaged velocity is less than 0.1 m/s, with a relative error below 10%. The mean error in current direction does not exceed 30°, corresponding to a relative error also under 10%. These metrics demonstrate that the ROMS model can accurately reproduce the tidal current processes and their spatiotemporal characteristics within the complex nearshore bathymetry of the Bohai and Yellow Seas, exhibiting sound simulation accuracy and stability.

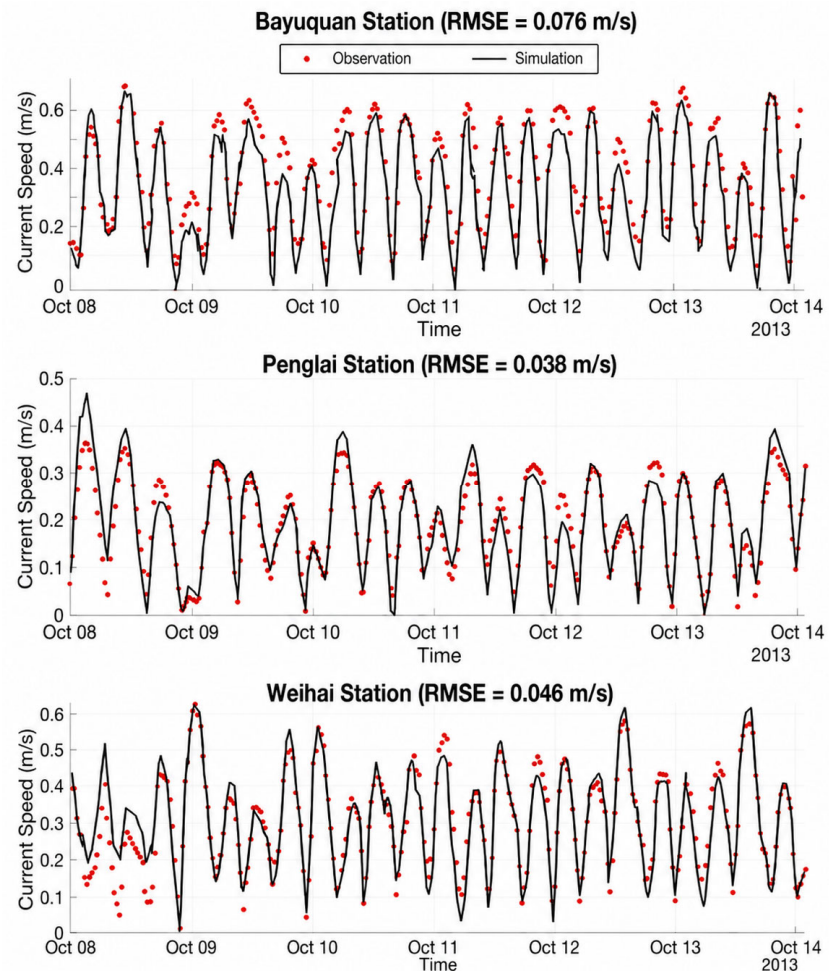


Figure 4. Comparisons of modeled and observed tidal velocities at validation points.

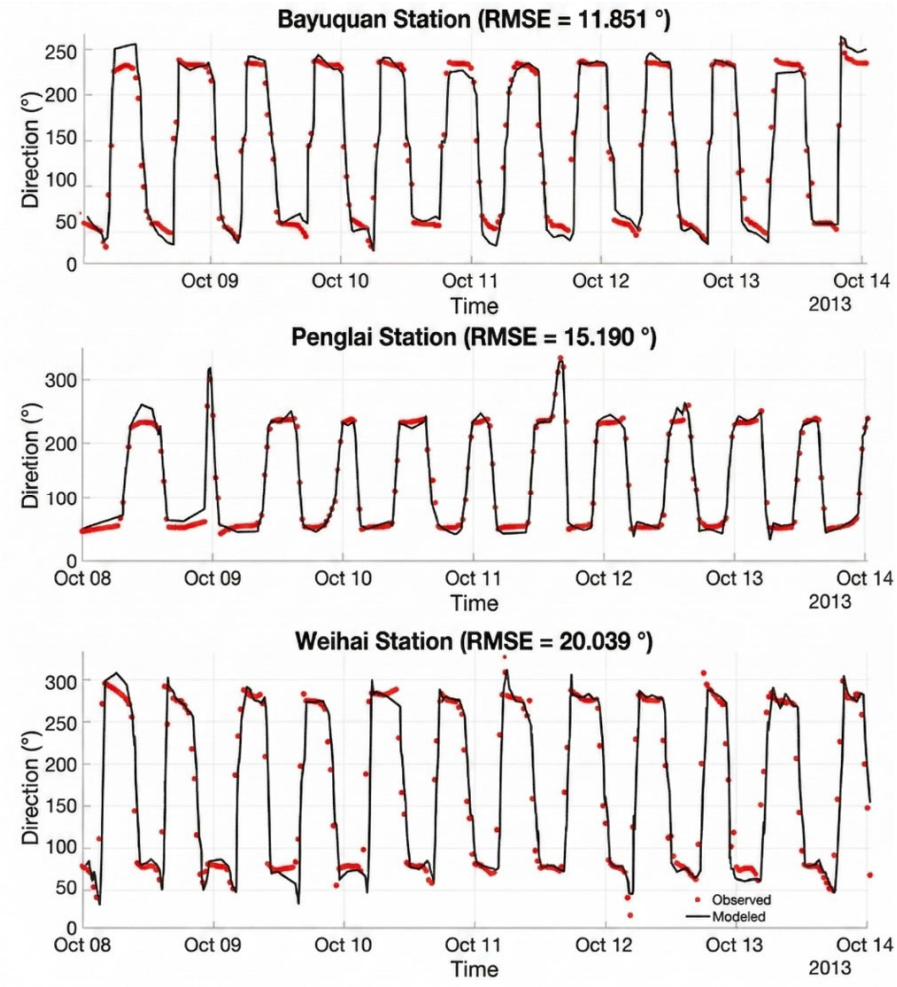


Figure 5. Comparisons of modeled and observed tidal direction at validation points.

Overall, the validation results indicate that the established ROMS model can reasonably reproduce the dominant tidal elevation variations and depth-averaged tidal current characteristics at the available observation stations, providing a basis for regional-scale theoretical tidal current energy assessment. However, it should also be noted that the available ADCP observations are spatially limited relative to the full extent of the Bohai and Yellow Seas. In particular, the present validation dataset cannot fully cover narrow channels, headland regions, and high-gradient nearshore areas where tidal current energy estimates are most sensitive to velocity errors. Therefore, the simulated current velocities and derived power densities in local hotspot areas should be interpreted as theoretical hydrodynamic estimates, and further site-specific ADCP observations are recommended before turbine-array design or engineering deployment.

3.3. Tidal Current Characteristics in the Bohai and Yellow Seas

The tidal current regime in the Bohai and Yellow Seas exhibits diverse characteristics, influenced by multiple factors including geographical latitude, water depth, bathymetry, and coastline configuration. The primary tidal current types include regular semi-diurnal, irregular semi-diurnal, and diurnal currents. Specifically, regular semi-diurnal currents dominate in parts of the Bohai Bay and Laizhou Bay, where the flow field remains relatively stable. In contrast, the central Bohai Sea displays irregular semi-diurnal currents, with more complex dynamic features due to various environmental influences. For instance, irregular diurnal currents are observed near Longkou owing to localized topography, increasing the complexity of current simulation.

Along the coastlines of the Bohai and Yellow Seas, tidal currents typically exhibit a rectilinear (alongshore-alternating) flow pattern (Figure 6). During flood tides, currents flow generally westward north of the peninsula and southwestward to the south; the directions reverse during ebb tides. This distinct flow structure affects the distribution and utilization of nearshore marine resources.

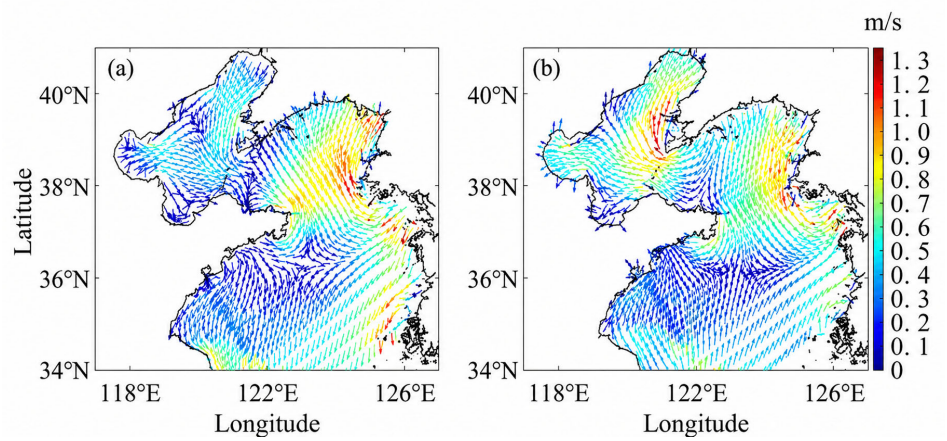


Figure 6. Schematic diagram of flood tidal current fields (**a**) and ebb tidal current fields (**b**) in the Yellow and Bohai Seas.

From the perspective of hydrodynamic characterization, regions with more regular tidal current patterns provide useful reference conditions for model evaluation and resource comparison. However, theoretical tidal current energy availability depends not only on tidal current type, but also on current magnitude, effective flow duration, effective water depth, and local bathymetric controls. Therefore, reliable resource assessment requires high-resolution hydrodynamic simulations and long-term time series analysis rather than inference from tidal current type alone.

4. Results and Discussion

4.1. Spatiotemporal Characteristics of Tidal Current Energy in the Bohai and Yellow Seas

Based on the validated astronomical tide model and the tidal current energy assessment methodology, long-term numerical simulations of tidal currents in the Bohai and Yellow Seas were conducted for the period 2010–2020. The simulated data were averaged seasonally and annually to systematically analyze the temporal and spatial characteristics of the tidal currents. By integrating current velocity, direction, and spatial distribution, annual and seasonal theoretical tidal current energy indicators across the study area were derived. The spatiotemporal patterns and variation laws of the tidal current power density across the study area were further investigated.

4.1.1. Tidal Current Power Density

Common assessment methods that estimate extractable tidal-stream energy, such as turbine-array or flux-based approaches, usually require site-specific information on turbine layout, device characteristics, blockage effects, and extraction feedback. Such information is not available at the regional screening stage of the present study. Therefore, this study uses power density as a hydrodynamic indicator of the undisturbed theoretical kinetic energy flux of tidal currents. The calculated power density does not include turbine power coefficients, device-specific power curves, wake losses, array interactions, blockage effects, or flow reduction induced by energy extraction. Accordingly, the reported values should be interpreted as theoretical hydrodynamic resource availability rather than technically exploitable or economically recoverable energy.

In this context, power density is used as a general hydrodynamic metric for comparing the spatial distribution and relative intensity of undisturbed theoretical tidal current energy resources. Therefore, this study employs power density as the core indicator for assessment and comparative analysis. The formulations are as follows:

The average power density is given by the following:

$$P_{mean} = \frac{1}{2}\rho\overline{V^3}, \tag{44}$$

where P_{mean} is the average power density, ρ is seawater density (taken as 1025 kg/m^3), and V is the average tidal current velocity.

The peak power density is expressed as follows:

$$P_{peak} = \frac{1}{2}\rho\overline{V_{peak}^3}, \tag{45}$$

where P_{peak} is the peak power density and V_{peak} is the peak tidal current velocity.

The effective power density is defined as follows:

$$P_e = \frac{1}{2}\rho V_e^3, \tag{46}$$

where P_e is the effective power density and V_e is the effective tidal current velocity with the selected baseline threshold of 0.5 m/s.

In this study, mean power density, peak power density, and effective power density all refer to theoretical power density indicators derived from the undisturbed simulated current field. They are used to compare hydrodynamic resource intensity and persistence among different regions, not to estimate actual turbine electrical output. The peak power density is defined as the maximum instantaneous theoretical kinetic energy flux during the simulation period. It is used to identify short-term high-energy tidal phases and local tidal acceleration, rather than sustained power availability. Therefore, peak power density should be interpreted together with annual mean power density and threshold-dependent effective flow duration.

The velocity threshold of 0.5 m/s used in this study should be regarded as a baseline screening threshold rather than a universal turbine cut-in speed. Actual tidal current converters differ in cut-in velocity, rated velocity, power curve, rotor diameter, control strategy, and deployment depth. Therefore, the effective flow duration and effective water depth calculated here are threshold-dependent hydrodynamic indicators. If a different turbine technology is considered, the threshold should be recalculated using device-specific operating characteristics.

4.1.2. Spatiotemporal Distribution Characteristics of Tidal Currents and Power Density in the Bohai and Yellow Seas

This section provides a detailed analysis of the spatiotemporal characteristics of tidal currents and their power density, focusing on the dynamic seasonal variations and spatial distribution patterns. Depth-averaged current velocities were used to ensure consistency and representativeness.

The seasonal variation in tidal currents was analyzed by dividing the year into spring (March–May), summer (June–August), autumn (September–November), and winter (December–February). The results indicate that the overall seasonal difference in tidal current velocity across the Bohai and Yellow Seas is not pronounced (Figure 7). The variation in the seasonal mean velocity is generally small in the main high-energy areas, with differences in most areas below 0.05–0.1 m/s. This suggests that the first-order spatial

pattern of tidal current energy in these areas is primarily controlled by astronomical tidal forcing, bathymetry, and coastline geometry. However, this does not imply that seasonal hydrographic processes are negligible. Seasonal stratification, river discharge variability, and monsoon-driven residual circulation may still influence local vertical shear, nearshore residual currents, and resource stability, particularly in shallow bays, estuarine waters, and sediment-rich coastal areas.

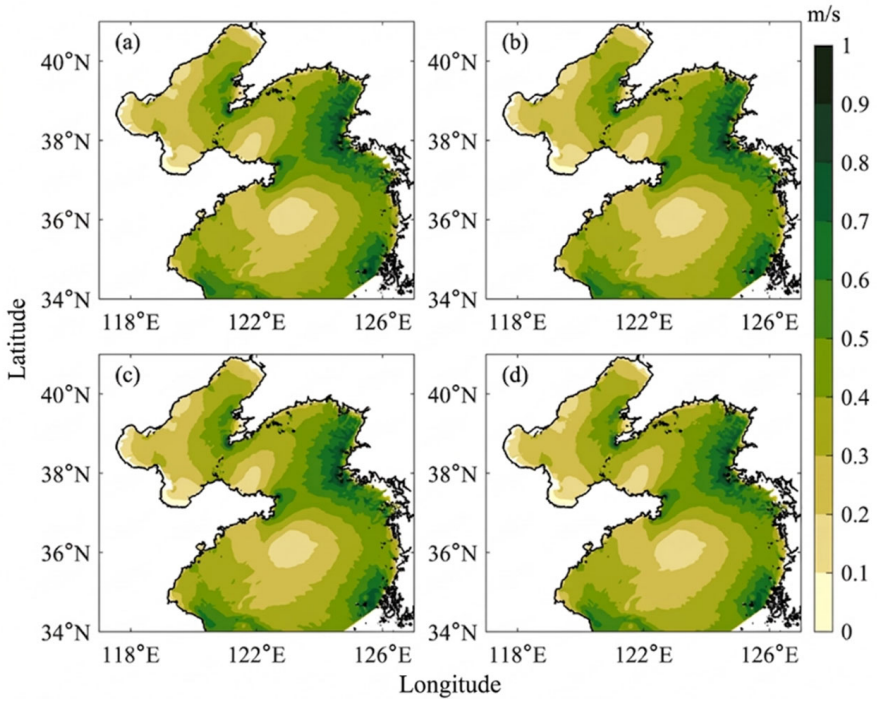


Figure 7. Seasonal average tidal current velocity distributions. (**a**) Spring average tidal current velocity distribution; (**b**) summer average tidal current velocity distribution; (**c**) autumn average tidal current velocity distribution; (**d**) winter average tidal current velocity distribution.

It should also be noted that seasonal mean fields do not fully describe the temporal variability relevant to tidal energy engineering. Tidal current energy is inherently intermittent because current speed varies over flood–ebb, spring-neap, monthly, and seasonal timescales. Extreme hydrodynamic events such as storm surges and typhoon-induced currents may also temporarily modify current speed, water level, and device loading conditions. The present study focuses on multi-year theoretical resource characterization using seasonal means, annual means, effective flow duration, and representative hourly power density time series. More detailed exceedance-probability statistics, low-energy interval analysis, and extreme-event simulations should be conducted in future engineering-oriented assessments.

The spatial distributions of the annual mean tidal current velocity and the corresponding power density are shown in Figure 8. The annual mean velocity across the region generally ranges from 0 to 1 m/s but exhibits a marked east–west disparity (Figure 8a). The eastern Yellow Sea, particularly along the west coast of the Korean Peninsula, shows mean velocities mostly above 0.5 m/s, indicating relatively strong theoretical hydrodynamic resource intensity. In contrast, the western Yellow Sea, especially along the south coast of the Shandong Peninsula, typically exhibits mean velocities below 0.3 m/s, reflecting relatively weak theoretical resource intensity. Besides the Korean Peninsula coast, notable high-velocity areas (locally exceeding 0.8 m/s) are identified near Chengshantou (Shandong Province) and the west of Lvshun (Liaoning Province).

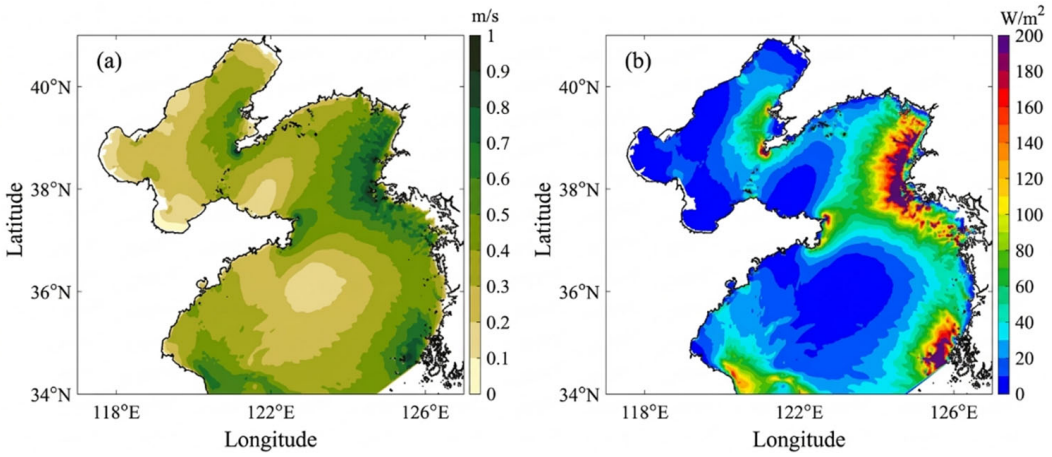


Figure 8. Annual average tidal current velocity distribution map (**a**) and tidal current energy power density distribution map (**b**).

The spatial pattern of the annual mean power density closely aligns with the velocity distribution (Figure 8b). Apart from the aforementioned resource-favorable areas (Korean Peninsula coast, the coast of northern Jiangsu, Chengshantou, and west of Lvshun), the power density in most other areas is below 30 W/m^2. The power density in these key zones exceeds 100 W/m^2, indicating favorable theoretical hydrodynamic resource characteristics. Overall, the tidal current power density in the Bohai and Yellow Seas exhibits a distinct "high in the east, low in the west" pattern. Resource-favorable areas are mainly concentrated along the west coast of the Korean Peninsula, the southwestern Liaodong Peninsula, the eastern Shandong Peninsula, and the coastal waters of Jiangsu Province, and these areas may be considered candidates for further site-specific assessment.

4.2. Multi-Index Diagnostic Assessment of Theoretical Tidal Current Energy Resources

A multi-index diagnostic assessment of theoretical tidal current energy resources in the Bohai and Yellow Seas was conducted using several complementary hydrodynamic indicators: annual mean theoretical power density, peak theoretical power density, threshold-dependent effective flow duration, and effective water depth. These indicators were not combined into a single weighted suitability score in the present study, because the appropriate weights depend strongly on turbine type, device operating range, foundation requirements, environmental constraints, navigation restrictions, grid accessibility, and project objectives. Instead, the indicators were interpreted jointly to distinguish different hydrodynamic resource characteristics, including high-intensity hotspots, persistent moderate-energy areas, and depth-limited regions.

In this diagnostic approach, annual mean theoretical power density represents the background resource intensity; peak theoretical power density identifies short-term high-energy tidal phases and local acceleration zones; threshold-dependent effective flow duration characterizes the temporal persistence of currents exceeding the selected velocity threshold; and effective water depth reflects the vertical extent of potentially usable flow. Since some of these indicators are physically interrelated through current velocity, they should not be interpreted as independent criteria in a formal multi-criteria decision-making model. Their combined use is intended to provide a more complete hydrodynamic description than any single indicator alone.

Using 0.5 m/s as the baseline screening threshold, the time during which the current velocity exceeds this threshold is defined as the effective flow duration. Vertically, the thickness of the water column where the velocity exceeds the same threshold is defined as the effective water depth. These two indicators are used to describe the persistence and

vertical extent of potentially usable tidal currents under the selected threshold, rather than to represent a universal turbine operating criterion.

The calculated spatial distribution of the annual mean effective water depth is shown in Figure 9a. The waters west of Lvshun (Dalian, Liaoning Province), east of Chengshantou (Rongcheng, Shandong Province), and along the west coast of the Korean Peninsula generally exhibit effective water depths exceeding 25 m, with localized areas surpassing 70 m. These results indicate a relatively large vertical extent of currents exceeding the baseline threshold. In contrast, the coastal area of northern Jiangsu Province shows smaller effective water depth, typically around 15 m, suggesting a shallower but more spatially extensive moderate flow regime. Whether these vertical flow conditions can support turbine deployment depends on turbine dimensions, foundation type, navigation constraints, seabed conditions, and environmental requirements.

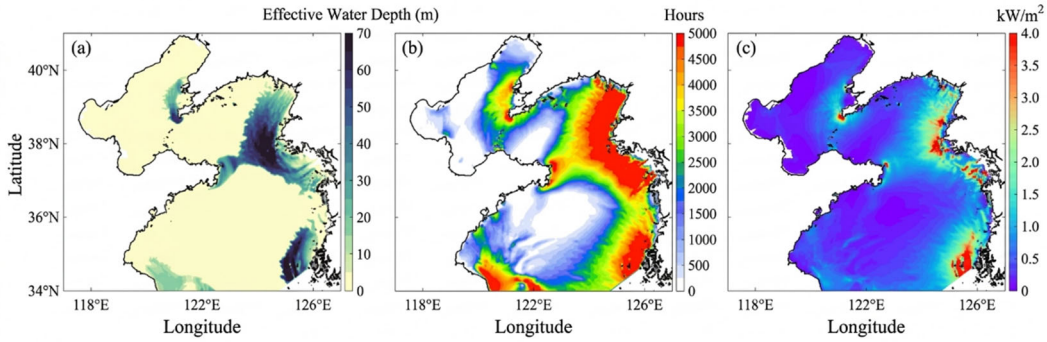


Figure 9. Spatial distributions of tidal current energy indicators; (**a**) annual mean effective water depth; (**b**) annual cumulative effective flow duration; (**c**) annual peak theoretical power density.

The calculated annual cumulative effective flow duration (Figure 9b) exceeds 5000 h in key areas, including west of Lvshun, east of Chengshantou, the northeastern coast of Jiangsu, and the west coast of the Korean Peninsula. This threshold-dependent indicator suggests relatively persistent energetic-flow conditions, but it should not be interpreted as sustained turbine power output. Conversely, regions like Bohai Bay, Laizhou Bay, and the central South Yellow Sea show durations of less than 500 h, indicating limited persistence of currents exceeding the selected threshold.

Furthermore, the calculated spatial distribution of the annual peak power density (Figure 9c) reveals significant local disparities. Values exceed 4 kW/m^2 in the prime areas west of Lvshun, east of Chengshantou, and along the west coast of the Korean Peninsula, indicating strong local theoretical hydrodynamic intensity. The coastal area of northern Jiangsu shows values around 1 kW/m^2, while most other regions are below 0.5 kW/m^2, indicating relatively weak theoretical hydrodynamic resource intensity under the present assessment metrics. Synthesizing the metrics of effective water depth, cumulative flow duration, and power density, the coastal waters of China within the Bohai and Yellow Seas with favorable theoretical hydrodynamic resource characteristics are primarily concentrated west of Lvshun, east of Chengshantou, and the northeastern coastal region of Jiangsu Province.

In summary, the main favorable hydrodynamic resource areas are characterized by different combinations of theoretical power density, effective flow duration, and effective water depth. Laotieshan and Chengshantou represent high-intensity but spatially localized resource regimes, whereas the northern Jiangsu coast represents a lower-intensity but relatively persistent shallow-water regime. These differences suggest that the identified areas should be treated as candidate zones for further site-specific technical, environmental, and economic assessment, rather than as confirmed development sites.

4.3. Analysis of Representative Hydrodynamic Resource Areas

4.3.1. Hydrodynamic Setting and Formation Mechanisms

Three representative areas were selected to illustrate distinct theoretical hydrodynamic resource regimes: the west of Laotieshan, the east of Chengshantou, and the northern Jiangsu coastal area. The formation of these regimes can be explained by the combined effects of bathymetry, coastline geometry, and tidal-wave propagation. West of Laotieshan Cape, tidal exchange between the Bohai Sea and the northern Yellow Sea is constrained by the Bohai Strait and adjacent headland topography, producing local flow convergence and acceleration. East of Chengshantou, the protruding headland of the Shandong Peninsula modifies tidal-wave propagation and compresses the alongshore flow, generating strong rectilinear currents and high local power density. Along the northern Jiangsu coast, the broad shallow-water environment and gentle bathymetric gradients lead to lower peak intensity but more spatially uniform and persistent moderate currents. These differences indicate that the identified hotspots reflect distinct tide–topography interaction mechanisms rather than isolated numerical maxima. A systematic analysis of the tidal dynamic features and power density for these three regions is presented below.

4.3.2. Tidal Current Fields

The flood current field west of Laotieshan (Figure 10a) is primarily from the southeast with velocities generally exceeding 1 m/s, reaching up to 2 m/s in localized high-flow zones. During ebb tide (Figure 10d), the main flow direction reverses to northwest, with overall velocities mostly below 0.5 m/s, though local speeds can still reach 2 m/s due to topographic effects. The flood current field east of Chengshantou (Figure 10b) shows a dominant southerly flow, with local velocities surpassing 2 m/s. The ebb current field (Figure 10e) is characterized by a north–northwesterly flow, with local velocities adjusted by dynamics exceeding 1.5 m/s. In the northern Jiangsu area, the flood current field (Figure 10c) exhibits a relatively uniform velocity distribution with a dominant southeasterly flow, influenced by regional topography. The ebb current field (Figure 10f) shows a northwesterly flow with a velocity distribution consistent with the flood phase.

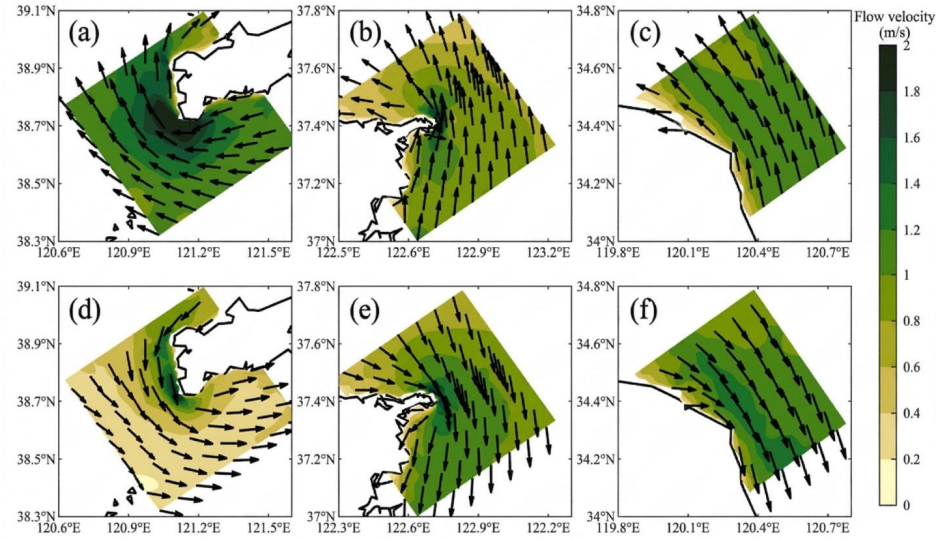


Figure 10. Flood and ebb current fields in representative hydrodynamic resource areas; (**a**) flood current west of Laotieshan Cape; (**b**) flood current east of Chengshantou; (**c**) flood current in the northern Jiangsu coastal area; (**d**) ebb current west of Laotieshan Cape; (**e**) ebb current east of Chengshantou; (**f**) ebb current in the northern Jiangsu coastal area.

The spatial distributions of effective water depth are shown in Figure 11a–c. The area west of Laotieshan shows effective water depths exceeding 70 m, with the extent of such depths being significantly larger than in the other two areas. The area east of Chengshantou has localized depths over 70 m, with a regional average around 35 m. In contrast, the northern Jiangsu area has effective water depths below 20 m. The distributions of annual effective flow duration are presented in Figure 11d–f. All three areas have localized durations exceeding 6000 h. The durations are concentrated in the west of Laotieshan and east of Chengshantou, while the distribution is more uniform across the northern Jiangsu area, with a regional average exceeding 4000 h.

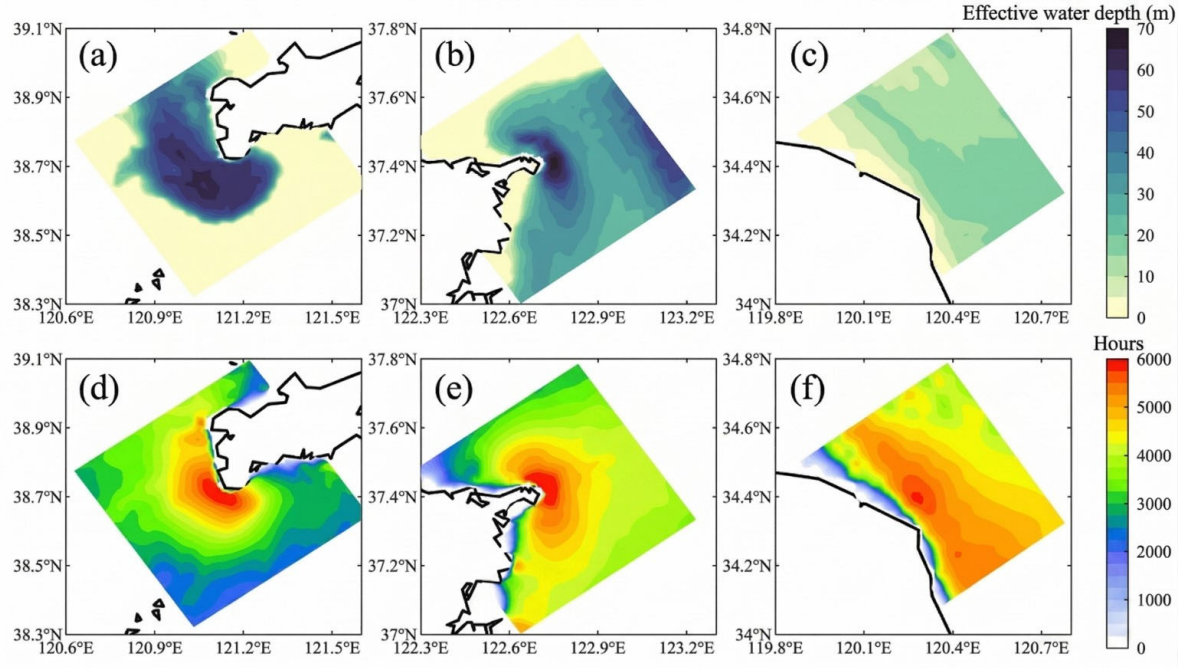


Figure 11. Spatial distributions of effective water depth and annual effective flow duration in representative hydrodynamic resource areas; (**a**–**c**) effective water depth west of Laotieshan Cape, east of Chengshantou, and in the northern Jiangsu coastal area; (**d**–**f**) annual effective flow duration in the corresponding areas.

4.3.3. Average and Peak Power Density

The spatial distributions of average and peak power density are shown in Figure 12. Regarding average power density (Figure 12a–c), the west of Laotieshan and east of Chengshantou both contain localized zones exceeding 400 W/m^2, but exhibit significant spatial heterogeneity with some areas below 50 W/m^2. In contrast, the northern Jiangsu area shows a more uniform distribution, predominantly in the range of 50–150 W/m^2. The peak power density (Figure 12d–f) locally exceeds 4 kW/m^2 in both the west of Laotieshan and east of Chengshantou, indicating strong local theoretical hydrodynamic intensity, although both also contain extensive low-value zones (<0.5 kW/m^2 and <0.25 kW/m^2, respectively), highlighting significant spatial disparity. The northern Jiangsu area shows a more homogeneous peak power density, distributed between 0 and 1 kW/m^2, suggesting relatively uniform moderate flow conditions despite lower peak intensity.

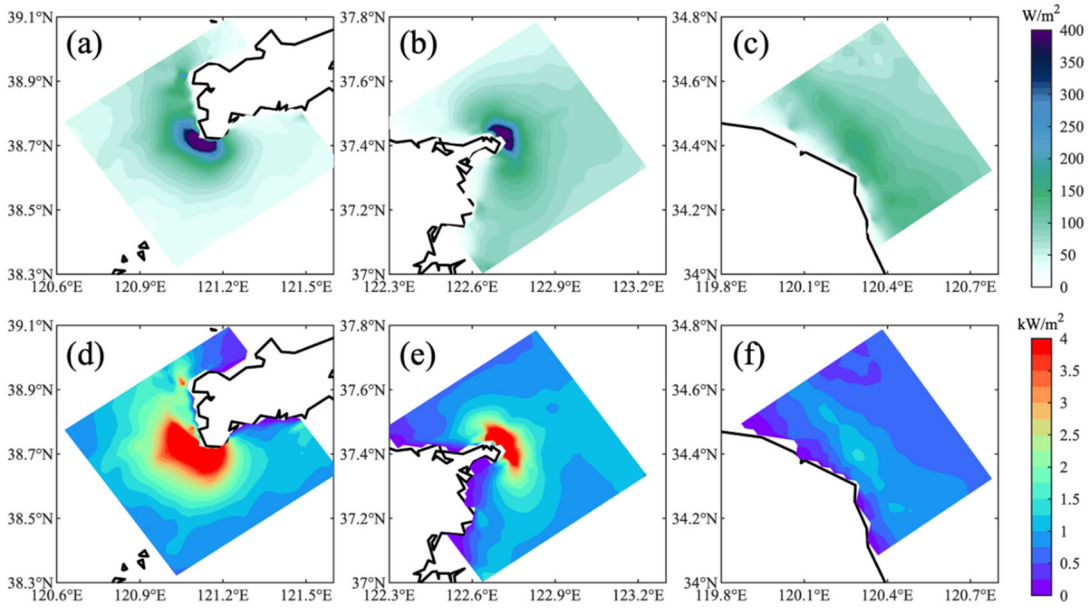


Figure 12. Distribution of average power density of tidal current energy in Laotieshan Cape (**a**), east of Chengshantou (**b**), and Northern Jiangsu region (**c**), distribution of peak power density of tidal current energy in Laotieshan Cape (**d**), east of Chengshantou (**e**), and Northern Jiangsu region (**f**).

This indicates a significant difference in hydrodynamic resource patterns: the former two areas represent high-intensity but spatially heterogeneous hotspots, whereas the latter represents a lower-intensity but more spatially uniform resource regime. Whether these patterns can be converted into efficient turbine deployment strategies requires further turbine-array modeling, wake-loss assessment, environmental screening, and site-specific engineering evaluation.

Characteristic points with the highest annual mean velocity in each region were selected for detailed analysis: west of Laotieshan (121.1263° E, 38.7099° N), east of Chengshantou (122.7267° E, 37.4038° N), and northern Jiangsu (120.2860° E, 34.3862° N). The tidal current roses for these points (Figure 13) reveal the dominant flow directions. At the Laotieshan point, the main directions are east–southeast (flood) and northwest (ebb), with flood velocities generally greater. At the Chengshantou point, the main directions are south/south–southwest (flood) and north–northwest (ebb), with flood dominance. At the northern Jiangsu point, the directions are southeast (flood) and northwest (ebb), with comparable flood and ebb velocities.

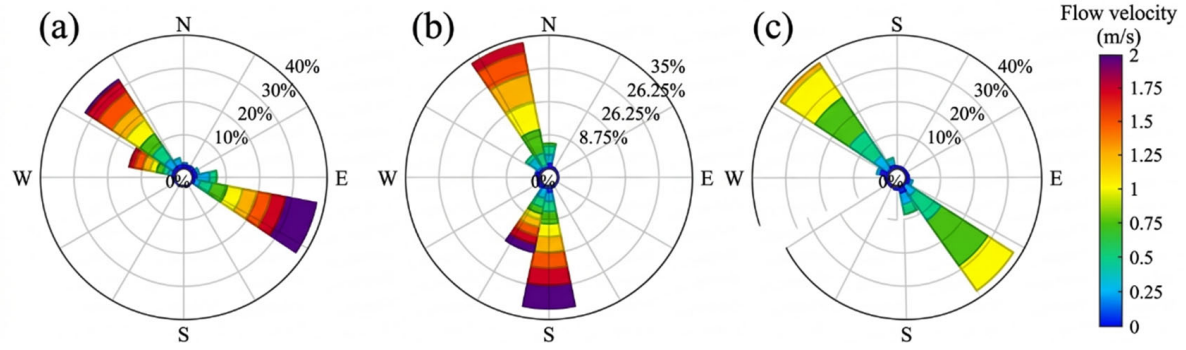


Figure 13. (**a**) Current rose diagram at west of Laotieshan Cape; (**b**) current rose diagram at east of Chengshantou; (**c**) current rose diagram at the northern Jiangsu coastal area.

4.3.4. Monthly Vertical Velocity and Power Density Time Series

The monthly averaged vertical velocity profiles at the three points (Figure 14) show relatively limited monthly variation and broadly consistent vertical distributions, with velocities exceeding the 0.5 m/s baseline screening threshold throughout most of the water column. At the Laotieshan and Chengshantou points, not only are the water depths greater, but monthly average velocities also exceed 0.8 m/s. The northern Jiangsu point has shallower depths and smaller velocities, ranging between 0.5 and 0.8 m/s.

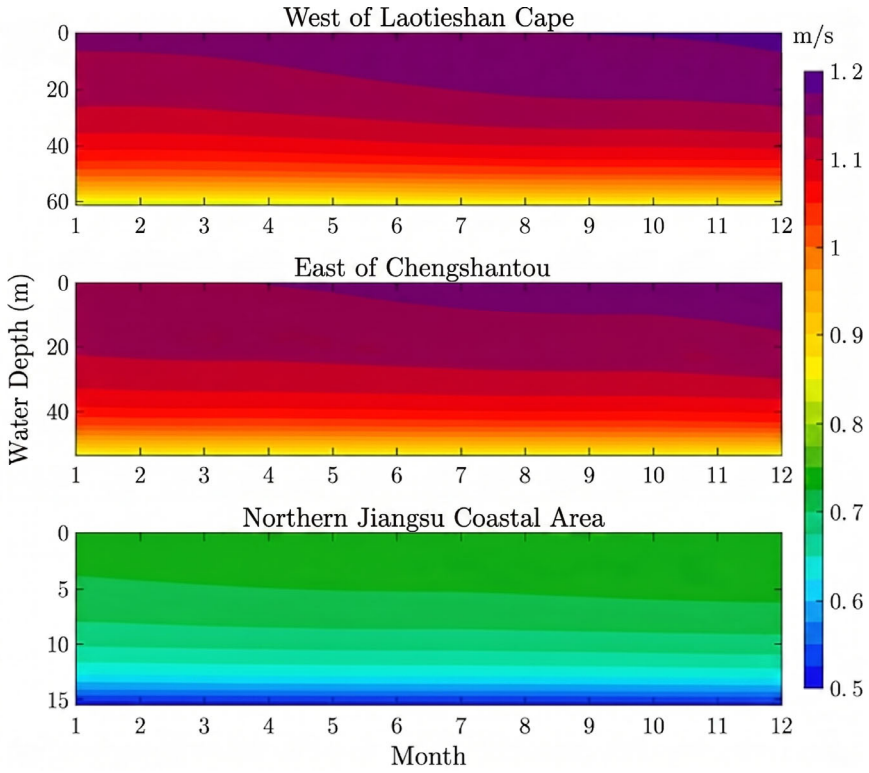


Figure 14. Monthly mean vertical current velocity profiles at representative points west of Laotieshan Cape, east of Chengshantou, and in the northern Jiangsu coastal area.

The hourly time series of instantaneous theoretical power density (Figure 15) further illustrates the intermittent nature of the tidal current resource. In the west of Laotieshan Cape, instantaneous power density can exceed 10 kW/m^2 during short high-energy tidal phases, while the values are substantially lower during weaker tidal phases. East of Chengshantou, peak values can reach approximately 8 kW/m^2, but these peaks should also be interpreted as short-term tidal maxima rather than sustained power levels. In the northern Jiangsu coastal area, instantaneous power density generally remains below 1.2 kW/m^2, indicating lower peak intensity but relatively persistent moderate flow conditions.

Therefore, the peak values reported in this study should not be used alone to infer practical extracted resources. They mainly indicate the intensity of local tidal acceleration under energetic tidal conditions. For preliminary resource screening, peak power density should be evaluated together with annual mean power density, threshold-dependent effective flow duration, and effective water depth. Device-specific power curves, turbine operating ranges, wake losses, and array interactions are required before estimating sustained power output or practically extractable energy.

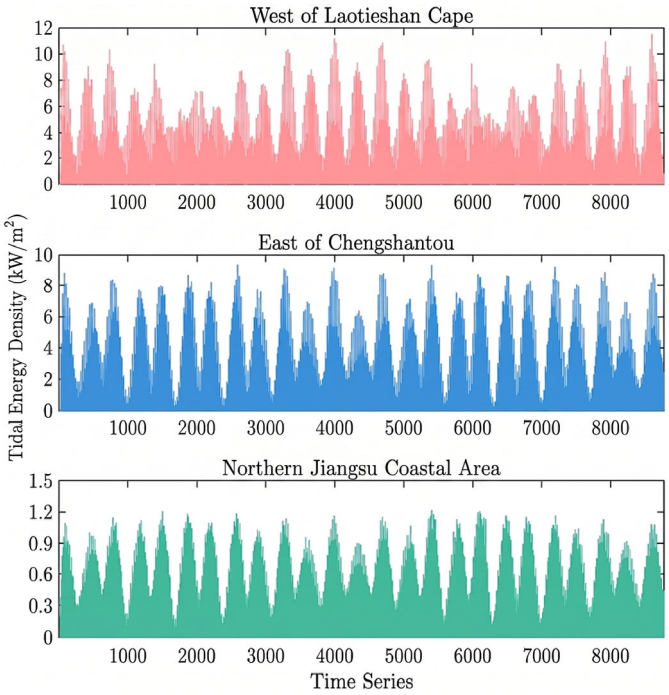


Figure 15. Hourly time series of instantaneous theoretical tidal current power density at representative points west of Laotieshan Cape, east of Chengshantou, and in the northern Jiangsu coastal area.

4.4. Limitations and Uncertainties

Several model-related uncertainties should be considered when interpreting the simulated tidal current velocities and derived theoretical power density. Bathymetric resolution and smoothing may affect the representation of narrow channels, steep slopes, and headland-controlled acceleration zones. Bottom friction parameterization influences tidal dissipation and near-bed velocity shear, while vertical turbulence closure affects the distribution of momentum over the water column. Open-boundary tidal forcing also controls the amplitude and phase of incoming tidal waves. Although the model was validated against available tide-gauge and ADCP observations, dedicated sensitivity experiments on bathymetry, bottom friction, turbulence closure, and boundary forcing were not conducted in the present study. Because theoretical power density scales with the cube of current speed, these model uncertainties may be amplified in local power density estimates.

The present analysis uses annual mean fields, seasonal mean fields, threshold-dependent effective flow duration, and representative hourly time series to describe resource persistence. However, these metrics do not fully resolve all forms of temporal variability relevant to engineering applications, including flood–ebb intermittency, spring-neap modulation, low-energy intervals, and extreme hydrodynamic events. Future work should conduct exceedance-probability analysis, duration-curve analysis, and storm-event simulations to better characterize operational availability and device loading conditions.

The 0.5 m/s velocity threshold adopted in this study is used as a baseline screening value, not as a universal turbine cut-in speed. Different tidal current turbines have different power curves, cut-in velocities, rated velocities, cut-out velocities, rotor diameters, and control strategies. Therefore, the effective flow duration and effective water depth reported here are threshold-dependent hydrodynamic indicators only. This study does not estimate annual energy production or capacity factor because such calculations require device-specific power curves, turbine availability, array spacing, wake losses, and operational control assumptions. Future work should combine the simulated velocity time series with

representative commercial turbine power curves to estimate annual energy production and capacity factors.

It is important to distinguish theoretical hydrodynamic resource availability from technically exploitable and practically recoverable tidal energy. The present study quantifies the undisturbed theoretical kinetic energy flux based on simulated current velocities. It does not include turbine power coefficients, device-specific power curves, cut-in/rated/cut-out velocities, wake recovery, array interaction losses, blockage effects, turbine availability, maintenance downtime, or flow reduction due to energy extraction. In real tidal current farms, energy extraction by turbines modifies the local momentum balance and can reduce downstream velocities, thereby decreasing the extractable energy relative to the undisturbed theoretical resource. Therefore, the reported power density values should be regarded as a theoretical hydrodynamic screening metric only.

Practical deployment also requires constraints that are not included in the present hydrodynamic assessment, including shipping lanes, anchorage areas, port operations, fisheries and aquaculture activities, marine protected areas, ecological sensitivity, seabed cables and pipelines, sediment mobility, foundation conditions, grid connection distance, and construction and maintenance costs. These constraints may significantly modify the suitability ranking of hydrodynamically favorable areas. Therefore, the hotspots identified in this study should be regarded as candidate hydrodynamic resource areas requiring subsequent marine spatial planning, environmental assessment, and techno-economic analysis.

Seasonal hydrographic variability represents another source of uncertainty. The Bohai and Yellow Seas are affected by seasonal stratification, river discharge variability, and monsoon-driven circulation. These processes may alter vertical mixing, bottom boundary layer structure, residual currents, and the vertical distribution of tidal current speed. Their effects are expected to be more pronounced in shallow bays, estuaries, river-influenced coastal waters, and sediment-rich regions than in strongly tide-dominated headland or strait areas. Because the present study focuses on a regional-scale theoretical resource assessment over the Bohai and Yellow Seas, it does not explicitly isolate the individual contributions of stratification, river discharge, and monsoon-driven residual circulation. Future work should conduct process-oriented sensitivity experiments and targeted field observations in representative estuarine and nearshore areas to evaluate their impacts on long-term resource stability.

The simulations were conducted using fixed present-day bathymetry and coastline geometry. Long-term sea-level rise, shoreline evolution, reclamation, dredging, sediment transport, and morphodynamic feedback were not included. These processes may alter tidal propagation, shallow-water friction, resonance characteristics, and flow constriction over the lifetime of a tidal energy project, especially in shallow and sediment-rich coastal regions such as northern Jiangsu and estuarine areas. Therefore, the identified resource patterns should be interpreted as present-day theoretical hydrodynamic conditions rather than fixed long-term development conditions.

4.5. Comparison with Previous Regional Assessments

The spatial pattern identified in this study is generally consistent with previous regional tidal current energy assessments, which reported high-energy areas near the Bohai Strait, the eastern Shandong Peninsula, and selected nearshore channels. For example, Yuan et al. reported peak power densities of approximately 6.2 kW/m^2 east of Shandong and 5.5 kW/m^2 in the Bohai Strait, which are comparable to the high-intensity areas identified near Chengshantou and Laotieshan in the present study. Differences in reported magnitudes may be related to model resolution, bathymetric datasets, open-boundary forcing, current-depth treatment, statistical definitions of peak power density, and whether the

results represent theoretical kinetic energy flux or extractable resource estimates. Compared with previous studies, the present assessment further combines annual mean theoretical power density, peak theoretical power density, effective flow duration, effective water depth, current roses, and vertical velocity structure to distinguish different hydrodynamic resource regimes.

5. Conclusions

This study developed a high-resolution, three-dimensional ROMS-based diagnostic assessment of theoretical tidal current energy resources in the Bohai and Yellow Seas. The results show that the first-order spatial pattern of tidal current energy is mainly controlled by astronomical tidal forcing, bathymetry, and coastline geometry. High theoretical resource intensity is concentrated west of Laotieshan Cape and east of Chengshantou, while the northern Jiangsu coast shows a lower-intensity but relatively persistent moderate-resource regime.

The annual mean theoretical power density in selected high-energy areas can exceed 100 W/m^2, and the cumulative annual effective flow duration can exceed 5000 h. Short-term instantaneous theoretical power density can exceed 10 kW/m^2 west of Laotieshan Cape and reach approximately 8 kW/m^2 east of Chengshantou during energetic tidal phases. These peak values reflect strong local tidal acceleration, but they should not be interpreted as sustained or directly extractable power.

The multi-index diagnostic assessment indicates that Laotieshan and Chengshantou are high-intensity but spatially heterogeneous hydrodynamic resource areas, whereas the northern Jiangsu coast is characterized by lower intensity but relatively persistent and spatially uniform flow conditions. These areas may be considered candidate zones for further site-specific assessment. However, the present study quantifies only the undisturbed theoretical hydrodynamic resource. Turbine power curves, wake effects, array interactions, environmental constraints, navigation safety, sediment dynamics, grid accessibility, capacity factors, and techno-economic feasibility remain to be evaluated before practical development decisions can be made.

Future work should combine high-resolution hydrodynamic simulations with expanded ADCP observations, uncertainty and sensitivity analyses, turbine-performance modeling, marine spatial constraints, and long-term bathymetric and sea-level change scenarios to support more complete technical and practical tidal current energy assessments.

Author Contributions: Conceptualization, Z.W. and B.L.; methodology, Z.W. and B.J.; software, Z.W. and N.Y.; validation, B.J. and L.S.; formal analysis, Z.W. and N.Y.; investigation, Z.W.; resources, X.X.; data curation, X.X.; writing—original draft preparation, Z.W.; writing—review and editing, Z.W. and X.X.; visualization, L.S.; supervision, N.Y. and B.L.; project administration, L.S. and B.L.; funding acquisition, Z.W. and X.X. All authors have read and agreed to the published version of the manuscript.

Funding: This research was funded by the National Natural Science Foundation of China (52571319) and Shandong Provincial Natural Science Foundation, China (ZR2022QD074).

Data Availability Statement: The original contributions presented in this study are included in the article. Further inquiries can be directed to the corresponding author.

Conflicts of Interest: Author Bo Jing was employed by the company Sinopec Shengli Oilfield. Author Xingyu Xu was employed by the company Sinopec Shengli Oilfield Branch Technical Testing Center and Sinopec (Shandong) Testing and Evaluation Research Co., Ltd. The remaining authors declare that the research was conducted in the absence of any commercial or financial relationships that could be construed as a potential conflict of interest.

References

1. Neill, S.P.; Haas, K.A.; Thiébot, J.; Yang, Z. A review of tidal energy—Resource, feedbacks, and environmental interactions. *J. Renew. Sustain. Energy* **2021**, *13*, 062702. [CrossRef]
2. Wen, Y.; Low, Y.M. Assessment of tidal stream energy and decarbonization potential by high-resolution simulations: A case study for Singapore. *Energy Convers. Manag.* **2026**, *348*, 120771. [CrossRef]
3. Liu, X.; Chen, Z.; Si, Y.; Qian, P.; Wu, H.; Cui, L.; Zhang, D. A review of tidal current energy resource assessment in China. *Renew. Sustain. Energy Rev.* **2021**, *145*, 111012. [CrossRef]
4. Zhang, D.; Ma, C. Utilization of tidal current and wave energy to help implement the carbon emissions peak and carbon neutrality strategy in China. *IOP Conf. Ser. Earth Environ. Sci.* **2022**, *983*, 012055. [CrossRef]
5. Melikoglu, M. Current status and future of ocean energy sources: A global review. *Ocean Eng.* **2018**, *148*, 563–573. [CrossRef]
6. Blunden, L.S.; Bahaj, A.S. Tidal energy resource assessment for tidal stream generators. *Proc. Inst. Mech. Eng. Part A J. Power Energy* **2007**, *221*, 137–146. [CrossRef]
7. Wang, F.; Zhang, J.; Guo, Y.; Luo, M.; Lin, Y.; Ji, Y.; Liu, S. Numerical study on the effects of combined wave, current, and wind on the tide and wave hydrodynamic field in the Yellow–Bohai Sea area, China. *Appl. Ocean Res.* **2025**, *165*, 104794. [CrossRef]
8. Yuan, S.; Yuan, P.; Sia, X.; Liu, X.; Tan, J.; Wang, S. Assessment of tidal current energy in Bohai Sea and Yellow Sea, China. *Indian J. Geo-Mar. Sci.* **2021**, *50*, 445–453. [CrossRef]
9. Garrett, C.; Cummins, P. The power potential of tidal currents in channels. *Proc. R. Soc. A* **2005**, *461*, 2563–2572. [CrossRef]
10. Work, P.A.; Haas, K.A.; Defne, Z.; Gay, T. Tidal stream energy site assessment via three-dimensional model and measurements. *Appl. Energy* **2013**, *102*, 510–519. [CrossRef]
11. Ramos, V.; Carballo, R.; Álvarez, M.; Sánchez, M.; Iglesias, G. Assessment of the impacts of tidal stream energy through high-resolution numerical modeling. *Renew. Energy* **2013**, *61*, 541–554. [CrossRef]
12. Li, D.; Wang, S.; Yuan, P. An overview of development of tidal current in China: Energy resource, conversion technology and opportunities. *Renew. Sustain. Energy Rev.* **2010**, *14*, 2896–2905. [CrossRef]
13. Robins, P.E.; Neill, S.P.; Lewis, M.J.; Ward, S.L. Characterising the spatial and temporal variability of the tidal-stream energy resource over the northwest European shelf seas. *Appl. Energy* **2015**, *147*, 510–522. [CrossRef]
14. Defne, Z.; Haas, K.A.; Fritz, H.M. GIS-based multi-criteria assessment of tidal stream power potential: A case study for Georgia, USA. *Renew. Sustain. Energy Rev.* **2011**, *15*, 2310–2321. [CrossRef]
15. Wang, F.; Zhang, J.; Zhang, Q. Potential assessment of tidal stream energy in Weihai water, China. In Proceedings of the 31st International Ocean and Polar Engineering Conference, Rhodes, Greece, 20–25 June 2021; pp. 708–713.
16. Gao, P.; Zheng, J.; Zhang, J.; Zhang, T. Potential assessment of tidal stream energy around Hulu Island, China. *Procedia Eng.* **2015**, *116*, 871–879. [CrossRef]
17. Iglesias, G.; Sánchez, M.; Carballo, R.; Fernández, H. The TSE index—A new tool for selecting tidal stream sites in depth-limited regions. *Renew. Energy* **2012**, *48*, 350–357. [CrossRef]
18. Vázquez, A.; Iglesias, G. A holistic method for selecting tidal stream energy hotspots under technical, economic and functional constraints. *Energy Convers. Manag.* **2016**, *117*, 420–430. [CrossRef]
19. Lewis, M.; Neill, S.P.; Robins, P.E.; Hashemi, M.R. Resource assessment for future generations of tidal-stream energy arrays. *Energy* **2015**, *83*, 403–415. [CrossRef]
20. *PD IEC TS 62600-201:2025*; Marine Energy—Wave, Tidal and Other Water Current Converters—Part 201: Tidal Energy Resource Assessment and Characterization. International Electrotechnical Commission: Geneva, Switzerland, 2015.

Disclaimer/Publisher's Note: The statements, opinions and data contained in all publications are solely those of the individual author(s) and contributor(s) and not of MDPI and/or the editor(s). MDPI and/or the editor(s) disclaim responsibility for any injury to people or property resulting from any ideas, methods, instructions or products referred to in the content.